Published in final edited form as:
Mar Pollut Bull. 2023 November ; 196: 115558. doi:10.1016/j.marpolbul.2023.115558.

Assessing potential of the Geostationary Littoral Imaging and Monitoring Radiometer (GLIMR) for water quality monitoring across the coastal United States

Blake A. Schaeffer[a,*], **Peter Whitman**[b], **Ryan Vandermeulen**[c,d], **Chuanmin Hu**[e], **Antonio Mannino**[f], **Joseph Salisbury**[g], **Boryana Efremova**[h], **Robyn Conmy**[i], **Megan Coffer**[j,k], **Wilson Salls**[a], **Hannah Ferriby**[l], **Natalie Reynolds**[m]

[a]US EPA, Office of Research and Development, Durham, NC 27709, United States of America

[b]Oak Ridge Institute for Science and Education, US EPA, Durham, NC 27709, United States of America

[c]National Oceanic and Atmospheric Administration, National Marine Fisheries Service, Silver Spring, MD, United States of America

[d]Science Systems and Applications, Inc., Lanham, MD, United States of America

[e]College of Marine Science, University of South Florida, St. Petersburg, FL, United States of America

[f]National Aeronautics and Space Administration, Goddard Space Flight Center, Greenbelt, MD, United States of America

[g]University of New Hampshire, Durham, NH, United States of America

[h]GeoThinkTank, LLC, Miami, FL, United States of America

[i]US EPA, Office of Research and Development, Cincinnati, OH 45268, United States of America

[j]National Oceanic and Atmospheric Administration, NESDIS Center for Satellite Applications and Research, Greenbelt, MD, United States of America

[k]Global Science and Technology Inc., Durham, NC, United States of America

[l]Tetra Tech, Research Triangle Park, NC 27709, United States of America

[*]Corresponding author. schaeffer.blake@epa.gov (B.A. Schaeffer).

CRediT authorship contribution statement

Blake A. Schaeffer: Conceptualization, Writing – original draft, Writing – review & editing, Resources, Supervision, Project administration, Funding acquisition. **Peter Whitman:** Conceptualization, Methodology, Software, Formal analysis, Investigation, Writing – original draft. **Ryan Vandermeulen:** Data curation, Methodology, Software, Formal analysis, Validation, Writing – original draft. **Chuanmin Hu:** Writing – original draft, Validation. **Antonio Mannino:** Writing – original draft, Validation. **Joseph Salisbury:** Writing – original draft. **Boryana Efremova:** Formal analysis. **Robyn Conmy:** Writing – original draft, Writing – review & editing. **Megan Coffer:** Writing – original draft. **Wilson Salls:** Writing – original draft, Writing – review & editing. **Hannah Ferriby:** Writing – original draft. **Natalie Reynolds:** Writing – original draft.

Declaration of competing interest

Antonio Mannino reports financial support was provided by NASA. Joseph Salisbury reports financial support was provided by NASA.

[m]RTI International, Research Triangle Park, NC, United States of America

Abstract

The Geostationary Littoral Imaging and Monitoring Radiometer (GLIMR) will provide unique high temporal frequency observations of the United States coastal waters to quantify processes that vary on short temporal and spatial scales. The frequency and coverage of observations from geostationary orbit will improve quantification and reduce uncertainty in tracking water quality events such as harmful algal blooms and oil spills. This study looks at the potential for GLIMR to complement existing satellite platforms from its unique geostationary viewpoint for water quality and oil spill monitoring with a focus on temporal and spatial resolution aspects. Water quality measures derived from satellite imagery, such as harmful algal blooms, thick oil, and oil emulsions are observable with glint $<0.005\ sr^{-1}$, while oil films require glint $>10^{-5}\ sr^{-1}$. Daily imaging hours range from 6 to 12 h for water quality measures, and 0 to 6 h for oil film applications throughout the year as defined by sun glint strength. Spatial pixel resolution is 300 m at nadir and median pixel resolution was 391 m across the entire field of regard, with higher spatial resolution across all spectral bands in the Gulf of Mexico than existing satellites, such as MODIS and VIIRS, used for oil spill surveillance reports. The potential for beneficial glint use in oil film detection and quality flagging for other water quality parameters was greatest at lower latitudes and changed location throughout the day from the West and East Coasts of the United States. GLIMR scan times can change from the planned ocean color default of 0.763 s depending on the signal-to-noise ratio application requirement and can match existing and future satellite mission regions of interest to leverage multi-mission observations.

Keywords

Geostationary satellite remote sensing; Oil spill; Water quality; Monitoring; Glint; Management

1. Introduction

The quality of water is an important factor in supporting environmental health, human health, and economic prosperity (Cox et al., 2006; Dodds et al., 2009; Schaeffer et al., 2012; Stroming et al., 2020; Wheeler et al., 2012; Zhang et al., 2022). Water quality is defined by biological, physical, and chemical properties to support intended uses, such as drinking water, recreation, irrigation, and food production. Measures of biological, physical, and chemical indicators may include turbidity, chlorophyll-a, harmful algae, temperature, nutrients, and a range of contaminants. Some of these indicators, such as water clarity, chlorophyll-a, sediment, colored dissolved organic matter, harmful algae, and surface oil slicks, are optically active, meaning that they interact with light through absorption and scattering (IOCCG, 2018). These optically active indicators can be directly measured using optical satellite sensors, which provide dynamic and ephemeral event information across broad spatial and temporal scales. This becomes especially important for monitoring extreme events (IPCC, 2012; Seneviratne et al., 2021) where communities need timely information regarding changes in water quality.

Satellite remote sensing of water quality has historically focused on polar orbiting platforms such as Terra and Aqua Moderate Resolution Imaging Spectroradiometer (MODIS), Sentinel-3 Ocean and Land Colour Instrument (OLCI), and Suomi/NOAA-20 Visible Infrared Imaging Radiometer Suite (VIIRS) (Groom et al., 2019). There are also several planned future polar orbiting missions that continue this trend such as the Plankton, Aerosol, Cloud, ocean Ecosystem (PACE) mission, the Surface Biology and Geology (SBG) mission, and sequential launches for Sentinel-3 OLCI and Joint Polar Satellite System VIIRS. These polar orbiting missions provide global observations but are limited to, at most, one acquisition per location per day and are susceptible to cloud contamination at the time of acquisition. In addition to these limitations, optical satellite sensors also suffer from sun glint, which occurs at varying intensities depending on acquisition characteristics like viewing angle, time of year, latitude, and surface wind speed. Sun glint can negatively impact water measurements and methods to remove its effects from satellite imagery have variable success (Hu, 2011; Wang and Bailey, 2001). However, in some cases, glint can be beneficial for monitoring water quality, primarily in the case of detecting surface oil films due to the increased surface reflectance caused by oil-induced wave damping (Adamo et al., 2009; Hu et al., 2009; Hu et al., 2021).

Water quality events, such as oil spills, river plume discharge, tidal effects, and harmful algal blooms, are highly dynamic and may evolve on daily to hourly timescales (IOCCG, 2012, 2018; see Fig. 3.1). Fine-scale temporal and spatial satellite remote sensing observations could lead to more comprehensive monitoring by filling spatial and temporal gaps in observations from traditional polar orbiting ocean color satellites. The geostationary position provides several advantages compared to polar orbiting platforms, such as: higher revisit frequencies, longer integration times allowing for improved radiometric accuracy, and flexibility in dwell time, which is the amount of time the sensor focuses on a location. However, a notable disadvantage is a fixed viewing area, which is referred to as the field of regard (Ruddick et al., 2014).

Historically, geostationary satellites have focused on communications and meteorological applications, while polar orbiting satellites are typically leveraged for ocean color observations. Some geostationary satellites have been repurposed for water quality monitoring. Examples include the Japanese Geostationary Meteorological Satellite to derive chlorophyll and suspended matter (Ding et al., 2020; Hafeez et al., 2021; Xing et al., 2021), and the Geostationary Operational Environmental Satellite for cyanobacteria and light attenuation (Houskeeper et al., 2022; Hu and Feng, 2014). However, these repurposed geostationary missions often lack the spectral resolution and sensitivity required for more comprehensive water quality monitoring. In 2010, the Geostationary Ocean Color Imager (GOCI) was launched as the first geostationary satellite dedicated to ocean color applications and was positioned to monitor the Northeast Asia region (Ryu et al., 2012; Yang et al., 2010). GOCI was successfully applied towards monitoring colored dissolved organic matter (Seo et al., 2020), phytoplankton biomass indicators such as chlorophyll (Feng et al., 2021; Salisbury et al., 2021; Zhao et al., 2022) and cyanobacteria (Li et al., 2022; Wang et al., 2022), light attenuation (Zhang et al., 2021), photosynthetically active radiation (Hwang et al., 2022), particulate organic carbon (Liu et al., 2019; Wang et al.,

2021), seaweed (Shin et al., 2021), sewage (Hong et al., 2012), and suspended sediment (Chau et al., 2021; Choi et al., 2012; Du et al., 2021).

The Geostationary Littoral Imaging and Monitoring Radiometer (GLIMR) is a geostationary sensor funded by the National Aeronautics and Space Administration (NASA) Earth Venture Instrument program anticipated to launch within this decade (Salisbury et al., 2016). GLIMR will provide high frequency temporal measures within a day, 300 m spatial pixel resolution at the nadir point on Earth's surface directly below the satellite, and hyperspectral observations to quantify coastal ocean processes that vary on short temporal and spatial scales. GLIMR spectral resolution will range from ~1 nm to 15 nm for bands between 340 and 1040 nm. Bands will be aggregated to bandwidths of ~5 nm to 40 nm full width at half maximum as required to accommodate algorithm performance. The 2017–2027 Decadal Survey for Earth Science and Applications from Space report prioritized the importance of understanding changes to the structure, function, and biodiversity of Earth's aquatic ecosystems, surface biology, and changes of biogeochemical fluxes of aquatic ecosystems (NAS, 2018). GLIMR data have the potential to advance coastal science and improve management and hazard mitigation efforts that benefit human and environmental health by quantifying biogeochemical fluxes between and within the coastal zone ecosystems. Specifically, GLIMR may be used in response to harmful algal bloom and oil spill events of national significance. Harmful algal bloom events of national significance are defined by the Harmful Algal Bloom and Hypoxia Research and Control Act (U.S.A. Congress, 2019) as an "event that has had or will likely have a significant detrimental environmental, economic, subsistence use, or public health impact on an affected State." Considerations include toxicity, potential to spread, economic impact, relative size in relation to the past five occurrences on a recurrent or annual basis, and geographic scope. An oil spill of national significance is defined by the severity, size, location, impact to public and environmental health, and scope of the response effort (Coast Guard, 2021).

This study describes the planned technical specifications of GLIMR and focuses on initial questions relevant for management applications supporting water quality such as: (1) How often may water quality measures be available? (2) What is the spatial coverage given the unique geostationary positioning, and how is the spatial resolution relevant for emergency event response? (3) What new possibilities, such as event tracking, are offered by GLIMR given its unique ability to change dwell times, a feature not previously available with polar orbiting satellites?

2. Methodology

2.1. Satellite characteristics

GLIMR is scheduled to launch in the 2027 to 2028 timeframe. The sensor's planned field of regard, viewing geometry, spectral characteristics, and image quality requirements were provided by NASA's Goddard Space Flight Center. These data, in combination with information from existing geostationary satellites, were used to determine the usability of GLIMR for water quality applications. GLIMR is a geostationary satellite that is planned to provide 340–1025 nm hyperspectral data of aquatic ecosystems and sub-daily temporal resolution. GLIMR's angular spatial pixel resolution will be 8.4 μrad, which will result in

imagery with a ground sampling distance of 300 m at nadir. Image data captured by GLIMR will use a fixed grid projection based on the Geodetic Reference System 1980 ellipsoid and the viewing perspective of a satellite in geostationary orbit. The proposed baseline orbital position is 98° W, but it could be placed in an orbital position anywhere from 110° W to 86° W (Fig. 1). GLIMR's field of regard will be defined by Earth's limb, which will occur ~62° from the sub-satellite point. Within this field of regard, planned routine monitoring will consist of 1–1.5-h revisits in the Gulf of Mexico, and at least twice daily images of the coastal conterminous United States (CONUS), selected Caribbean regions, the Amazon River discharge region, equatorial Pacific upwelling features, and the South Pacific clear waters. GLIMR's viewing capabilities afford favorable imaging angles from ~50° N to 50° S and 40° to 155° W when positioned at 98° W.

GLIMR's proposed sampling design was used to determine the rapidity and frequency with which a region could be monitored by leveraging diurnal and annual variation in sun glint for ocean ecosystem applications. A satellite's scan time determines the rapidity and frequency with which a region can be monitored. GLIMR will not scan the entire field of regard multiple times per day and can be tasked to image specific smaller regions at high frequency. Each scan that GLIMR makes will take 0.763 s to complete. These scans will be comprised of 3072 pixels in the north-south direction and a single pixel in the east-west direction. Given that GLIMR's spatial resolution will be 8.4 μrad, GLIMR's field of view for each scan is up to 25.8 mrad in the north-south direction or 1.48°. The rectilinear area covered by each of these scans grows as the distance from nadir increases and with curvature of the Earth.

2.2. Computing sun glint

Normalized sun glint (L_{GN}) is the sun glint radiance received by a sensor regardless of incident solar radiance. It provides a comparative measure of sun glint intensity given sea surface roughness and the position of satellite relative to the sun (see Table 1 for a summary of symbols and definitions). L_{GN}, in units of sr^{-1}, was computed at 0.25° intervals across GLIMR's viewing extent to quantify its influence on future image acquisition efforts. Following the Cox and Munk (1954) method to calculate normalized sun glint, the slope probability density function (PDF, p) of the facets that contribute to sun glint were multiplied by functions that incorporate the sensor zenith angle θ, the surface tilt expression $\tan^2\beta$, and the Fresnel reflection coefficient $\rho(\omega)$ of the water surface for unpolarized light:

$$L_{GN} = \frac{\rho(\omega)}{4} p \frac{\left(1 + tan^2\beta\right)^2}{cos\theta} \quad (1)$$

The slope PDF of the facets that contribute to sun glint was expressed as a function of the surface tilt viewing geometry and sea surface roughness variance:

$$p = \frac{1}{\pi\sigma^2} exp\left(\frac{-tan^2\beta}{\sigma^2}\right)$$

(2)

where σ^2 is sea surface roughness variance as a linear function of wind speed W in m s^{-1}, and $\tan^2\beta$ is an expression of the surface tilt of a facet that reflects sunlight to the satellite sensor relative to a horizontal plane. Sea surface roughness variance is computed as:

$$\sigma^2 = 0.003 + 0.00512^{\star}W \tag{3}$$

The expression of surface tilt is computed as:

$$tan^2\beta = \frac{sin^2\theta_0 + sin^2\theta + 2\ sin\theta_0\ sin\theta\ cos\phi}{(cos\theta_0 + cos\theta)^2} \tag{4}$$

where θ is the sensor zenith angle, θ_0 is the solar zenith angle, and ϕ is the relative azimuth angle between the sensor and the sun.

2.2.1. Wind speed—Observed sun glint patterns are dependent on sea surface roughness, which has a linear relationship with wind speed (Eq. 3). Empirical wind speed data was acquired from the European Centre for Medium-Range Weather Forecasts (ECMWF) Reanalysis v5 (ERA5) product offered by the Copernicus Climate Change Service (Hersbach et al., 2023). Hourly estimates of the eastward (u) and northward (v) components of wind at an altitude of 10 m were acquired from ERA5 at 0.25° spatial resolution. Wind speed W in m s^{-1} was calculated from these components as:

$$W = \sqrt{u^2 + v^2} \tag{5}$$

2.2.2. Sun and satellite position—The position of the sun and satellite were required to calculate normalized sun glint. The sun's position was defined in terms of solar zenith and solar azimuth angles relative to a point on the Earth's surface following the method described by Meeus (1998) and outlined by Reda and Andreas (2004). Solar zenith angle was corrected for atmospheric refraction under average conditions (Meeus, 1998; Saimundsson, 1986; Wittman, 1997). The satellite's position was defined in terms of sensor zenith and sensor azimuth angles relative to a point on the Earth's surface following the spherical approximation presented in Soler and Eisemann (1994).

2.3. Minimum event area

An event area may be defined as a harmful algal bloom or oil spill event of national significance. The relationship between satellite spatial resolution and minimum observable event area was explored by scraping the marine pollution surveillance reports from 2011 through 2021 that were generated by the National Oceanic and Atmospheric Administration

(NOAA) National Environmental Satellite, Data, and Information Service (NESDIS). These reports use low to high temporal resolution satellite imagery to manually delineate the extent and, in some cases, estimate the thickness of oil slicks and emulsions. Each report includes the observed oil slick surface area and the satellite sensor that was used. This analysis was limited to reports that were generated using imagery from satellites with optical sensors, omitting those generated *via* synthetic aperture radar. Additionally, Planet's Planet-Scope satellite data were used to demonstrate impacts of pixel size on resolving an event at the Mississippi Canyon Block 20 Saratoga Platform (MC20) site in the Gulf of Mexico (28.94° N, 88.97° W). During Hurricane Ivan in September 2004, 28 wells at the MC20 site were destroyed, which led to persistent oil plumes and surface slicks. Planet data were collected at 3.7 m spatial resolution at nadir (Schaeffer et al., 2022) and rescaled to match the spatial resolution of various coarser resolution satellites, including GLIMR.

3. Results and discussion

3.1. Spatial resolution and viewing extent

GLIMR's spatial sampling is presently defined as ground sampling distance, which captures the expected maximum pixel resolution and determines the amount of detail within the imagery. GLIMR's finest resolution is 300 m, which occurs at its nadir viewing point at the equator. This increases with distance from the nadir point due to changes in viewing angle and curvature of the Earth (Fig. 2). Median pixel resolution in the Gulf of Mexico is 330 m and along the East and West Coasts of the United States increases to 363 m. Resolution is >1 km along the field of regard edge, with limited capability at Alaska due to the increased air mass factor (AMF) resulting from the extreme viewing and solar zenith angles through the atmosphere. Previous validation studies using data from the Aerosol Robotic Network limited AMF to below 3.1 and ocean color studies for the Geostationary Coastal and Air Pollution (GEOCAPE) mission recommended a restriction of AMF ≤ 5 (Pahlevan et al., 2014). Performance of atmospheric correction schemes are dependent on AMF values lower than 5, and error typically increases with increased AMF (IOCCG, 2010; Ruddick et al., 2014). Therefore, the AMF was conservatively limited to ≤4 in this study, similar to how polar orbiting ocean color data can measure at sensor zenith up to 70°, approximately corresponding to an AMF > 5 above 70°, but validation data are excluded beyond 60° sensor zenith due to potential for decreased data quality (Bailey and Werdell, 2006; Barnes and Hu, 2016). Similarly, missing observations due to cloud cover are more prevalent at high sensor zenith angles as cloud cover viewed at an oblique angle obstructs more of the Earth's surface than cloud cover viewed from directly overhead. The AMF ≤ 4 in this study was used to constrain the viewing extent of GLIMR for sun glint quantification.

3.2. Sun glint

The optimal bands for oil detection are dependent on oil type, where blue and ultraviolet wavebands are best for oil sheen and crude oil, and near-infrared and short-wave infrared are best for emulsified oil. GLIMR is proposed to provide hyperspectral remote-sensing reflectance at 15 nm bandwidths from 340 to 400 nm, 10 nm bandwidths from 400 to 720 nm and 40 nm bandwidths from 720 to 1025 nm. Minimum sun glint thresholds for detecting surface oil films of 10^{-5} to $10^{-6}sr^{-1}$ were needed to detect oil film presence using

MODIS and those above 10^{-6} to $10^{-7}sr^{-1}$ using VIIRS (Sun and Hu, 2016). This study used the lower limit threshold of $>10^{-5}$ sr^{-1} normalized sun glint defined by Sun and Hu (2016) for surface oil film detection and normalized sun glint <0.005 sr^{-1} for water quality products other than oil. NASA's Seaviewing Wide Field-of-view Sensor (SeaWiFS) Data Analysis System (SeaDAS) (Baith et al., 2001) is a comprehensive software package for the processing and quality control of a wide array of satellite data. The SeaDAS level 2 generator (L2gen) processing software implements a high glint quality flag using a threshold >0.005 sr^{-1} for any water quality derived measure (Hu et al., 2020; Wang and Bailey, 2001). Glint thresholds were mapped in two-hour increments for the December solstice (Fig. 3), June solstice (Fig. 4), and March and September equinoxes (Fig. 5). Geographic areas within the white dashed line met the glint requirements for detecting oil films, and areas represented in yellow were above the ocean color glint quality flag for deriving water quality measures. Areas without color within the field of regard were experiencing darkness.

December solstice glint (Fig. 3) dominated the southwest Pacific Ocean from zero to 6:00 Coordinated Universal Time (UTC), then the southern Atlantic Ocean, near the Brazil Basin, from 8:00 to 12:00 UTC, and finally the eastern Pacific Ocean from 14:00 to 22:00 UTC. June solstice glint (Fig. 4) dominated the northern Pacific Ocean from zero to 6:00 UTC and then the northern Atlantic Ocean from 8:00 to 14:00 UTC. The glint area moved into the Gulf of Mexico and southern Pacific Ocean from 16:00 to 20:00 UTC and then back to solely the Pacific Ocean at 22:00 UTC. March and September equinoxes (Fig. 5) had glint from zero to 22:00 UTC along the equator primarily in the Pacific Ocean, except from 8:00 to 14:00 UTC when glint was in the Atlantic Ocean. During the March and September equinoxes, only the hours from 4:00 to 8:00 UTC supported ocean color glint quality flag requirements. These areas were, as expected, along the equator, first in the western Pacific Ocean at 4:00 UTC and shifting to the Atlantic Ocean by 8:00 UTC. These results were supported by a previous study preparing for GEOCAPE, where summer months were influenced by greater sun glint than winter months and at lower latitudes (Feng et al., 2017). This study is unique from Feng et al. (2017) in that the present study area was the planned field of regard for geostationary orbit, inclusive of the entire western United States, and provided detailed time of day maps where glint was most likely to occur. The results from this study complement Feng et al. (2017) for water quality management applications by mapping areas most likely to be impacted by the glint quality flag, which is useful for assessing capabilities for oil film monitoring throughout the day. If glint was present in areas to the east during GLIMR's early morning, or to the west late in day, then scans of those areas would be possible without impacting the predefined observational schedule of 5–6 images per day of the Gulf of Mexico and 2–3 images per day of the East and West Coasts of the United States.

3.3. Minimum event size

NOAA NESDIS marine pollution surveillance reports were used to quantify the spatial resolution of the satellites used to report oil spill area and quantify if GLIMR's spatial resolution would be valuable for monitoring oil spills. NESDIS used a range of optical satellite sensors with various spatial resolution configurations, including 1.24 m WorldView-3, 1.8 m WorldView-2, 3 m PlanetScope, 10 m Sentinel-2, 15 m Advanced

Spaceborne Thermal Emission and Reflection Radiometer, 20 m Sentinel-1, 30 m Landsat, 250 m Terra and Aqua, and 375 m VIIRS. At the MC20 site, the median oil area from NOAA NESDIS marine pollution surveillance reports was 2.28 km^2 from 2016 through 2021 (Schaeffer et al., 2022). Oil slick widths are often reported <10 m wide (Brown and Fingas, 2001), with the largest slicks typically <30 m wide and up to 100 m long (Sun et al., 2016; Svejkovsky et al., 2016). Including all marine pollution surveillance reports from optical satellite sensors with up to 375 m spatial resolution, oil spill area ranged from 2 km^2 to ~100 km^2 from 2011 to 2021 (Fig. 6A). Locations of marine pollution surveillance reports were previously reported in Schaeffer et al. (2022; see Fig. 1). Based on this assessment of NESDIS marine pollution surveillance reports, the spatial resolution of GLIMR is well-suited for observing oil spills, particularly in the Gulf of Mexico (Fig. 6B). The increase of oiled area with coarser resolution satellites was also due to the coverage area difference, where high-resolution satellites only covered a small area, so the detected oil areas were smaller. Across GLIMR's entire field of regard with AMF ≤ 4.0, median pixel resolution was 391 m (25th quantile was 337 m and 75th quantile was 465 m). Across CONUS, median pixel resolution was 363 m (25th quantile was 345 m and 75th quantile was 385 m), and within the Gulf of Mexico, median pixel resolution was 330 m (25th quantile was 324 m and 75th quantile was 337 m). These median pixel sizes were similar to the spatial resolution of VIIRS, which has been frequently used for oil spill monitoring (Hu et al., 2015a; Sun et al., 2018). Coastal waters adjacent to CONUS would also likely be adequate in pixel resolution but may decline in utility as the monitoring location moves further away from the sensor nadir and pixel resolution approaches >400 m. GLIMR could potentially resolve 50 % of CONUS estuaries and 79 % of sub-estuaries, with a minimum of three pixels across and at the CONUS median pixel resolution of 363 m (Schaeffer and Myer, 2020). Oil spill monitoring was not limited in the field of regard to just areas meeting sun glint requirements because thick oil and oil emulsions were observable with glint below the 10^{-5} sr^{-1} threshold.

Resampled true color images from PlanetScope were used as a demonstration of spatial resolution on the observability of an oil slick at the MC20 site in the Gulf of Mexico (Fig. 7). The 3.7 m native resolution PlanetScope imagery was resampled to 4 m and then expanded by approximate orders of magnitude representing spatial resolutions similar to those from commercial sensors (4 m), land imagers (40 m), GLIMR within the field of regard (400 to 800 m), and for various other missions with coarser spatial resolution (2000 m). These images show how the pixel resolution affects the ability to observe surface oil slicks or other water quality events. While there is a clear distinction in the level of detail discernable with spatial resolutions increasing from 3.7 m to 400 m, GLIMR's pixel resolution still allows oil and non-oiled waters to be differentiated. Pixel scales at ≥800 m may not be appropriate spatial resolutions for smaller scale water quality events.

Coastal water quality spatial gradients are a fractal problem depending on the application need (Seuront and Lagadeuc, 1997). Previous studies have supported spatial resolutions similar to that of GLIMR up to 500 m as adequate for various coastal water quality applications (IOCCG, 1999, 2012). However, there are additional application needs spanning a range of resolutions, including finer spatial resolutions than that offered through GLIMR (Niemi et al., 2004; Schaeffer and Myer, 2020). Estuarine spatial gradient studies

of chlorophyll, colored dissolved organic matter, and dissolved organic carbon had the greatest changes within 300 m of coastal marsh (Tzortziou et al., 2011). Other studies indicated optimal resolution is <200 m within 10 km of land and expands to 1 km resolution offshore (Bissett et al., 2004; Moses et al., 2016). However, resolutions <1 km are still desired offshore to capture heterogeneous events such as frontal boundaries. GLIMR median pixel resolution of 363 m may allow resolution of these gradients at land-ocean exchanges and will improve the ability to quantify ephemeral and heterogenous events. For example, Aurin et al. (2013) demonstrated that >90 % of river plume dynamics were resolved with 520 m resolution, well within GLIMR specifications. GLIMR's increased resolution will also reduce uncertainties because traditional ocean color 1 km water quality measures are potentially underestimated in heterogenous waters such as ocean fronts, river plumes, and eddy features (Lee et al., 2012a).

3.4. Temporal considerations

Despite coarser spatial resolution than some polar orbiting platforms currently used for water quality applications (*i.e.*, 300 m Sentinel-3 and ≤ 60 m Sentinel-2), geostationary satellites provide improved temporal resolution and the potential for dynamic signal-to-noise ratios (SNR) across spectral bands by altering the integration (*i.e.*, dwell) time (Hu et al., 2012). The time in which GLIMR may acquire an image with similar spatial coverage of a polar orbiting platform depends on the swath width of that satellite. Table 2 provides estimated GLIMR scan times based on swath widths for existing and future polar orbiting platforms ranging from the largest swath of 3000 km with VIIRS to the smallest swath of 9 km with Maxar's WorldView Legion satellite constellation, launched in early 2023. The larger the swath width, the longer it would take GLIMR to rescan the equivalent width; it would take GLIMR 125.07 min to reproduce a VIIRS swath and 0.39 min to reproduce a WorldView Legion swath. The region of interest location impacts GLIMR's scan time—the further from GLIMR's nadir point (north/south or east/west), the shorter the scan time (Table 2). This was a result of viewing geometry where pixel size increased and, as a result, rectilinear area covered increased further from the nadir viewing point. It takes GLIMR 0.763 s to complete one scan, which consists of a single pixel in the east-west direction and 3072 pixels in the north-south direction using the ocean color default settings with a target SNR of 1000:1 spanning wavelengths from 415 nm to 580 nm at typical ocean top-of-atmosphere radiances.

While not explicitly assessed here, the spectral resolution of GLIMR will provide one of the most detailed space-based spectral datasets with a range of potential water quality applications. Lassalle et al. (2020) emphasized the need to make hyperspectral remote sensing an operational tool for monitoring oil contamination, as hyperspectral observations may allow for the characterization of oil slick thickness (Lennon et al., 2005) and perhaps even the differentiation of emulsified oil from surrounding waters. Vegetation health in impacted habitats can also be better characterized using hyperspectral remote sensing, although the relatively coarse spatial resolution of GLIMR may prevent adequate measurements in highly heterogenous systems (Lassalle et al., 2020). Dierssen et al. (2021) reviews potential improvements in aquatic remote sensing *via* hyperspectral imagery,

including phytoplankton pigment differentiation, wetland ecosystem fragmentation, and improved characterization of benthic communities.

Collectively, observations from both geostationary and polar orbiting satellites may be leveraged to provide multiple image acquisitions within a day to enhance temporal coverage of a water quality event (Minghelli et al., 2021). For example, a harmful algal bloom event could initially be identified with a polar orbiting platform. GLIMR could then be targeted to track that event until the next polar orbit provides a follow-up measurement either the following day, in the case of VIIRS or PACE, or several days later, such as with Sentinel-2 or Landsat.

While the ocean color default scan time is planned for 0.763 s for a default SNR specific to ocean color measurement requirements, alternative SNRs may be valuable depending on the application. Demonstrations of two alternate application scenarios were developed by creating a relative index of the scan time to represent a desired SNR through either doubling the scan time to 1.526 s or reducing the scan time by a factor of 0.7 which then reduces the default value to 0.534 s (Fig. 8). The default scan time yielded SNR of 1000:1 from 415 nm to 580 nm and between 750:1 and 500:1 from 650 nm to 800 nm. Doubling the scan time increased the SNR to 2000:1 from 415 nm to 580 nm and between 1160:1 and 1000:1 from 650 nm to 800 nm. Doubling the scan time may be beneficial for low signal events or to reduce uncertainties in ocean color measures. Reducing the scan time by a factor of 0.7 decreased SNR to 700:1 from 415 nm to 580 nm and 406:1 from 650 nm to 700 nm. A reduced scan time that retains an SNR near 400:1 in the visible spectrum would provide a binary detect or non-detect capability for events such as oil films (Qi et al., 2017) or *Sargassum* slicks (Hu et al., 2015b) while providing rapid targeted observations that may limit disruption of GLIMR planned operations. Managers may calculate the time required to reproduce the swath of another polar orbiting platform by multiplying the time reported in Table 2, in minutes, by the relative index factor shown in Fig. 8 to leverage both GLIMR and polar orbiting missions such as for the hypothetical management scenario described in the previous paragraph. For example, an oil spill or *Sargassum* event may be identified with PACE at GLIMR's sub-satellite point and GLIMR could be targeted to rescan that portion of the PACE swath for confirmation in that location. The GLIMR scan time may be reduced by a factor of 0.7 if only a detect and non-detect classification was required. Where GLIMR would take 111.36 min to reproduce the PACE swath using default ocean color scan time and SNR, the reduction of a 0.7 scan time reduced the amount of time GLIMR requires to reproduce the PACE swath to 77.95 min. The reduction in scan time may serve as a dual benefit either to allow for more measurements throughout the day to track a given event, or to allow for a return to the GLIMR predefined observational schedule of 5–6 images per day of the Gulf of Mexico and 2–3 images per day of the East and West Coasts of the United States. This is particularly beneficial when monitoring the extent of water quality events, which can change rapidly.

High sampling frequency is critical for monitoring coastal ocean biogeochemical processes and physically driven changes. Multi-day observations improve cloud avoidance and the number of water quality observations (Salisbury et al., 2016), and temporal uncertainties may be reduced in temporal composites with increased data coverage (Barnes and Hu,

2015). Repeated daily measures will improve resolution of particulate matter, dissolved matter, and carbon exchange budgets influenced by tidal transport (Cao et al., 2018). Diurnal dynamics of harmful algal blooms due to diel vertical migration and physical advection will be improved, as demonstrated by a study tracking the impacted area of a *Prorocentrum* harmful algal bloom using GOCI images (Lou and Hu, 2014). In a similar approach, *Trichodesmium* bloom size was reported to nearly quadruple in size within an eight-hour time frame (Hu and Feng, 2014). Primary productivity models will also improve with diurnal measures of physiology and irradiance (Lee et al., 2012b; Wu et al., 2022).

Variation in sensor view angle, solar position, AMF, wind speed, and time of year all impact the number of observation hours per day during which a quality image could be acquired for water quality monitoring applications. Temporally, ocean color water quality observation hours increased from January through April from an average of 7 to 10 h per day, with a peak average of 11 h per day along all United States' coasts from May through August (Fig. 9). Observation hours declined from September through December from an average of 10 to 7 h per day. The minimum observation hours occurred in December and the maximum occurred in July, corresponding to the December and June solstices. Spatially, ocean color water quality observation hours were an average of 1 h greater in the Gulf of Mexico and lower latitudes of the United States from December through April compared to higher latitudes. Higher latitudes on both United States East and West Coasts had fewer hours available for observation, especially approaching the northern United States and Canada border where viewing hours were negligible November through January. Overall, oil film observation hours were fewer than water quality hours, ranging from 0 to 7 h throughout the year (Fig. 10). Temporally, oil film quality observation hours increased March to April from an average of 3 to 6 h, with a peak average of 7 h in May and June. Optimal peak hours for oil film observation in the Gulf of Mexico were from 16:00 UTC through 18:00 UTC during the June solstice. Observation hours declined from 6 h in July to 2 h in September. No oil film observation hours were available from November to February.

3.5. Limitations

GLIMR may be considered a part of a larger, comprehensive management toolbox for water quality monitoring (El Serafy et al., 2021). There are technical limitations, as with any instrument, to be considered. For example, quantification of oil thickness is desired in many response applications, but optical satellites are limited in their ability to derive oil thickness, especially when compared to synthetic aperture radar. Cloud cover, smoke, and adverse weather conditions will still limit optical measures in geostationary orbit (Temitope Yekeen and Balogun, 2020). This study did not consider cloud cover interference as this has been adequately addressed in previous studies (Feng et al., 2017; Mercury et al., 2012; Schaeffer et al., 2022). The results presented in this study were based on current GLIMR designs and plans that may deviate within mission baseline and threshold ranges. Although the technical design has been completed, GLIMR could still face operational challenges. Faster scans are not likely an issue, nor are repeat scans of the same small region in rapid succession to increase scan time and SNR. Slower scans may be limited due to gimbal stability; an alternative solution may be to step and stare so integration time could be extended. Data latency is a consideration, especially for emergency management operations, such as during

oil spill and harmful algal bloom events. Finally, tasking requests must be prioritized by the science team; thus, tasking does not guarantee a given image acquisition request will be fulfilled.

4. Conclusions

This study details the technical specifications of GLIMR, the United States' first geostationary satellite for ocean color observations, and provides a framework for potential applications regarding water quality characterization and oil film monitoring following its launch later this decade. The spatial, temporal, and radiometric resolutions of GLIMR were evaluated and compared to currently operating satellites. GLIMR offers its best pixel resolution of 300 m directly below the satellite, median 391 m within an area with an AMF ≤ 4, and median 330 m spatial resolution across the Gulf of Mexico. GLIMR's spatial resolution is at the coarser end of the distribution of some satellite platforms used for water quality measurements but is within the range necessary for resolving oil spills, half of CONUS estuaries, and a majority of sub-estuaries. Meanwhile, temporal resolution is unmatched compared to polar orbiting sensors, with possible revisits up to six times per day and planned twice daily acquisitions of the coastal CONUS, among other regions. Radiometric resolution was assessed through SNR at the default scan time as well as at alternate scan times for replication of potential use cases. Across the visible wavelengths, SNR is expected to be sufficient for classifying oil detect and non-detect at the default scan time (0.763 s) as well as at double and 0.7 times this scan time.

Based on previously published sun glint thresholds, GLIMR is well suited for thick oil, oil emulsion, oil film detection, and water quality characterization across the Gulf of Mexico and the United States' East and West Coasts, particularly in the months surrounding the June solstice. Upon its launch into orbit, GLIMR can complement existing remote sensing efforts to identify oil spills in coastal waters, adding sub-daily observations to the suite of satellites currently leveraged by NOAA NESDIS for their marine pollution surveillance reports. Previous studies using imagery from GOCI demonstrate the benefits of sub-daily water quality measurements, including an improved understanding of spatiotemporal algal bloom dynamics (Choi et al., 2014). Sub-daily, hyperspectral observations from GLIMR may supplement existing water quality observations of lower latitude coastal areas. GLIMR has the potential to provide unprecedented observations of ocean color dynamics valuable for management applications, particularly when combined with current polar orbiting platforms.

Acknowledgements

This work was supported by the NASA Earth Venture Instrument Program 80LARC21DA002 and GLIMR WBS 259547.04.01. Work was also supported by the US EPA, and Oak Ridge Institute for Science and Education (ORISE). This article has been reviewed by the Center for Environmental Measurement and Modeling and approved for publication. Mention of trade names or commercial products does not constitute endorsement or recommendation for use by the US Government. The views expressed in this article are those of the authors and do not necessarily reflect the views or policies of the US EPA.

Data availability

All data and code will be made available at the following DOI after acceptance: doi: 1023719/1529553.

References

Adamo M, De Carolis G, De Pasquale V, Pasquariello G, 2009. Detection and tracking of oil slicks on sun-glittered visible and near infrared satellite imagery. Int. J. Remote Sens. 30, 6403–6427.

Aurin D, Mannino A, Franz B, 2013. Spatially resolving ocean color and sediment dispersion in river plumes, coastal systems, and continental shelf waters. Remote Sens. Environ. 137, 212–225.

Bailey SW, Werdell PJ, 2006. A multi-sensor approach for the orbit validation of ocean color satellite data products. Remote Sens. Environ. 102, 12–23.

Baith K, Lindsay R, Fu G, McClain CR, 2001. SeaDAS: data analysis system developed for ocean color satellite sensors. EOS Trans. Am. Geophys. Union 82, 202.

Barnes B, Hu C, 2015. Cross-sensor continuity of satellite-derived water clarity in the Gulf of Mexico: insights into temporal aliasing and implications for long-term water clarity assessment. IEEE Trans. Geosci. Remote Sens. 53, 1761–1772.

Barnes BB, Hu C, 2016. Dependence of satellite ocean color data products on viewing angles: a comparison between SeaWiFS, MODIS, and VIIRS. Remote Sens. Environ. 175, 120–129.

Bissett WP, Arnone RA, Davis CO, Dickey TD, Dye D, Kohler DDR, Gould RW, 2004. A look at ocean-color scales of variability, spatial coherence, and the need for fine-scale remote sensing in coastal ocean optics. Oceanography 17, 33–43.

Brown CE, Fingas MF, 2001. New space-borne sensors for oil spill response. In: International Oil Spill Conference Proceedings, pp. 911–916.

Cao F, Tzortziou M, Hu C, Mannino A, Fichot CG, Del Vecchio R, Najjar RG, Novak M, 2018. Remote sensing retrievals of colored dissolved organic matter and dissolved organic carbon dynamics in north American estuaries and their margins. Remote Sens. Environ. 205, 151–165.

Chau PM, Wang C-K, Huang A-T, 2021. The spatial-temporal distribution of GOCI-derived suspended sediment in Taiwan coastal water induced by typhoon Soudelor. Remote Sens. 13, 194.

Choi J-K, Park YJ, Ahn JH, Lim H-S, Eom J, Ryu J-H, 2012. GOCI, the world's first geostationary ocean color observation satellite, for the monitoring of temporal variability in coastal water turbidity. J. Geophys. Res. 117, C09004.

Choi J-K, Min J-E, Noh JH, Han T-H, Yoon S, Park YJ, Moon J-E, Ahn J-H, Ahn SM, Park J-H, 2014. Harmful algal bloom (HAB) in the East Sea identified by the Geostationary Ocean color imager (GOCI). Harmful Algae 39, 295–302.

Coast Guard US, 2021. National incident commander's manual for spill of national significance management. In: Security, U.S.D.o.H. Commandant United States Coast Guard, Washington, DC.

Congress, U.S.A., 2019. National Integrated Drought Information System Reauthorization Act of 2018. In: Congress. PL, Washington, DC, pp. 115–423.

Cox C, Munk W, 1954. Measurement of the roughness of the sea surface from photographs of the sun's glitter. J. Opt. Soc. Am. 44, 838.

Cox ME, Johnstone R, Robinson J, 2006. Relationships between perceived coastal waterway condition and social aspects of quality of life. Ecol. Soc. 11, 35–59.

Dierssen HM, Ackleson SG, Joyce KE, Hestir EL, Castagna A, Lavender S, McManus MA, 2021. Living up to the hype of hyperspectral aquatic remote sensing: science, resources and outlook. Frontiers in Environmental Science 9.

Ding X, He X, Bai Y, Zhu Q, Gong F, Li H, Li J, 2020. High-frequency and tidal period observations of suspended particulate matter in coastal waters by AHI/Himawari-8. Opt. Express 28, 27387–27404.

Dodds WK, Bouska WW, Eitzmann JL, Pilger TJ, Pitts KL, Riley AJ, Schloesser JT, Thornbrugh DJ, 2009. Eutrophication of U.S. freshwaters: analysis of potential economic damages. Environ. Sci. Technol. 43, 12–19. [PubMed: 19209578]

Du Y, Wang D, Zhang J, Wang YP, Fan D, 2021. Estimation of initial conditions for surface suspended sediment simulations with the adjoint method: a case study in Hangzhou Bay. Cont. Shelf Res. 227, 104526.

El Serafy GYH, Schaeffer BA, Neely M-B, Spinosa A, Odermatt D, Weathers KC, Baracchini T, Bouffard D, Carvalho L, Conmy RN, Keukelaere LD, Hunter PD, Jamet C, Joehnk KD, Johnston JM, Knudby A, Minaudo C, Pahlevan N, Reusen I, Rose KC, Schalles J, Tzortziou M, 2021. Integrating inland and coastal water quality data for actionable knowledge. Remote Sens. 13.

Feng C, Ishizaka J, Saitoh K, Mine T, Zhou Z, 2021. Detection and tracking of Chattonella spp. and Skeletonema spp. blooms using geostationary ocean color Imager (GOCI) in Ariake Sea, Japan. J. Geophys. Res. Oceans 126 e2020JC016924.

Feng L, Hu C, Barnes BB, Mannino A, Heidinger AK, Strabala K, Iraci LT, 2017. Cloud and Sun-glint statistics derived from GOES and MODIS observations over the intra-Americas sea for GEO-CAPE mission planning. J. Geophys. Res. Atmos. 122, 1725–1745.

Groom S, Sathyendranath S, Ban Y, Bernard S, Brewin R, Brotas V, Brockmann C, Chauhan P, Choi J-K, Chuprin A, Ciavatta S, Cipollini P, Donlon C, Franz B, He X, Hirata T, Jackson T, Kampel M, Krasemann H, Lavender S, Pardo-Martinez S, Mélin F, Platt T, Santoleri R, Skakala J, Schaeffer B, Smith M, Steinmetz F, Valente A, Wang M, 2019. Satellite ocean colour: current status and future perspective. Front. Mar. Sci. 6.

Hafeez S, Wong MS, Abbas S, Jiang G, 2021. Assessing the potential of geostationary Himawari-8 for mapping surface Total suspended solids and its diurnal changes. Remote Sens. 13, 336.

Hersbach H, Bell B, Berrisford P, Biavati G, Horányi A, Muñoz Sabater J, Nicolas J, Peubey C, Radu R, Rozum I, Schepers D, Simmons A, Soci C, Dee D, Thépaut J-N, 2023. ERA5 hourly data on single levels from 1940 to present. In: CDS. C.C.C.S.C.S.C.D.S.

Hong GH, Yang DB, Lee H-M, Yang SR, Chung HW, Kim CJ, Kim Y-I, Chung CS, Ahn Y-H, Park Y-J, Moon J-E, 2012. Surveillance of waste disposal activity at sea using satellite ocean color imagers: GOCI and MODIS. Ocean Science Journal 47, 387–394.

Houskeeper HF, Hooker SB, Cavanaugh KC, 2022. Spectrally simplified approach for leveraging legacy geostationary oceanic observations. Appl. Opt. 61, 7966–7977. [PubMed: 36255917]

Hu C, 2011. Observing MODIS ocean color patterns under severe sun glint. In: Proc. SPIE 8030, Ocean Sensing and Monitoring III 80300M.

Hu C, Feng L, 2014. GOES imager shows diurnal changes of a *Trichodesmium erythraeum* bloom on the West Florida shelf. IEEE Geosci. Remote Sens. Lett. 11, 1428–1432.

Hu C, Li X, Pichel WG, Muller-Karger FE, 2009. Detection of natural oil slicks in the NW Gulf of Mexico using MODIS imagery. Geophys. Res. Lett. 36.

Hu C, Feng L, Lee Z, Davis CO, Mannino A, McClain CR, Franz BA, 2012. Dynamic range and sensitivity requirements of satellite ocean color sensors: learning from the past. Appl. Opt. 51, 6045–6062. [PubMed: 22945151]

Hu C, Chen S, Wang M, Murch B, Taylor J, 2015a. Detecting surface oil slicks using VIIRS nighttime imagery under moon glint: a case study in the Gulf of Mexico. Remote Sensing Letters 6, 295–301.

Hu C, Feng L, Hardy RF, Hochberg EJ, 2015b. Spectral and spatial requirements of remote measurements of pelagic Sargassum macroalgae. Remote Sens. Environ. 167, 229–246.

Hu C, Barnes BB, Feng L, Wang M, Jiang L, 2020. On the interplay between ocean color data quality and data quantity: impacts of quality control flags. IEEE Geosci. Remote Sens. Lett. 17, 745–749.

Hu C, Lu Y, Sun S, Liu Y, 2021. Optical remote sensing of oil spills in the ocean: what is really possible? Journal of Remote Sensing 2021, 1–13.

Hwang DJ, Frouin R, Tan J, Ahn J-H, Choi J-K, Moon J-E, Ryu J-H, 2022. Algorithm to estimate daily PAR at the ocean surface from GOCI data: description and evaluation. Front. Mar. Sci. 9, 924967.

IOCCG, Yoder JA., 1999. Status and Plans for Satellite Ocean-Colour Missions: Considerations for Complementary Missions. IOCCG, Dartmouth, Canada.

IOCCG, 2010. In: Wang M. (Ed.), Atmospheric Correction for Remotely-Sensed Ocean Colour Products. Dartmouth, Canada, p. 78.

IOCCG, 2012. Ocean-colour observations from a geostationary orbit. In: Antoine D. (Ed.), Reports of the International Ocean-Colour Coordinating Group. IOCCG, Dartmouth, Canada.

IOCCG, 2018. Earth Observations in Support of Global Water Quality Monitoring. IOCCG, Dartmouth, Canada.

IPCC, 2012. Managing the Risks of Extreme Events and Disasters to Advance Climate Change Adaptation. A Special Report of Working Groups I and II of the Intergovernmental Panel on Climate Change. Cambridge University Press, New York, NY, USA.

Lassalle G, Fabre S, Credoz A, Dubucq D, Elger A, 2020. Monitoring oil contamination in vegetated areas with optical remote sensing: a comprehensive review. J. Hazard. Mater. 393, 122427.

Lee Z, Hu C, Arnone R, Liu Z, 2012a. Impact of sub-pixel variations on ocean color remote sensing products. Opt. Express 20, 20844–20854.

Lee Z, Jiang M, Davis C, Pahlevan N, Ahn Y-H, Ma R, 2012b. Impact of multiple Satellite Ocean color samplings in a day on assessing phytoplankton dynamics. Ocean Science Journal 47, 323–329.

Lennon M, Thomas N, Mariette V, Babichenko S, Mercie G, 2005. Oil slick detection and characterization by satellite and airborne sensors: experimental results with SAR, hyperspectral and lidar data. In: Proceedings 2005 IEEE International Geoscience and Remote Sensing Symposium IGARSS, 2005, p. 4.

Li J, Li Y, Bi S, Xu J, Guo F, Lyu H, Dong X, Cai X, 2022. Utilization of GOCI data to evaluate the diurnal vertical migration of Microcystis aeruginosa and the underlying driving factors. J. Environ. Manag. 310, 114734.

Liu D, Bai Y, He XQ, Tao BY, Pan DL, Chen CTA, Zhang L, Xu Y, Gong CH, 2019. Satellite estimation of particulate organic carbon flux from Changjiang River to the estuary. Remote Sens. Environ. 223, 307–319.

Lou X, Hu C, 2014. Diurnal changes of a harmful algal bloom in the East China Sea: observations from GOCI. Remote Sens. Environ. 140, 562–572.

Meeus J, 1998. Atmospheric Refraction., Astronomical Algorithms, 2nd edition. Willmann-Bell, Inc., Richmond, VA, pp. 105–108.

Mercury M, Green R, Hook S, Oaida B, Wu W, Gunderson A, Chodas M, 2012. Global cloud cover for assessment of optical satellite observation opportunities: a HyspIRI case study. Remote Sens. Environ. 126, 62–71.

Minghelli A, Chevalier C, Descloitres J, Berline L, Blanc P, Chami M, 2021. Synergy between low earth orbit (LEO)-MODIS and geostationary earth orbit (GEO)-GOES sensors for sargassum monitoring in the Atlantic Ocean. Remote Sens. 13.

Moses WJ, Ackleson SG, Hair JW, Hostetler CA, Miller WD, 2016. Spatial scales of optical variability in the coastal ocean: implications for remote sensing and in situ sampling. J. Geophys. Res. Oceans 121, 4194–4208.

NAS, 2018. Thriving on our Changing Planet: A Decadal Strategy for Earth Observation from Space. The National Academies Press, Washington, DC.

Niemi G, Wardrop D, Brooks R, Anderson S, Brady V, Paerl H, Rakocinski C, Brouwer M, Levinson B, McDonald M, 2004. Rationale for a new generation of indicators for coastal waters. Environ. Health Perspect. 112, 979–986. [PubMed: 15198917]

Pahlevan N, Lee Z, Hu C, Schott JR, 2014. Diurnal remote sensing of coastal/oceanic waters: a radiometric analysis for geostationary coastal and air pollution events. Appl. Opt. 53, 648–665. [PubMed: 24514182]

Qi L, Lee Z, Hu C, Wang M, 2017. Requirement of minimal signal-to-noise ratios of ocean color sensors and uncertainties of ocean color products. J. Geophys. Res. Oceans 122, 2595–2611.

Reda I, Andreas A, 2004. Solar position algorithm for solar radiation applications. Sol. Energy 76, 577–589.

Ruddick K, Neukermans G, Vanhellemont Q, Jolivet D, 2014. Challenges and opportunities for geostationary ocean colour remote sensing of regional seas: a review of recent results. Remote Sens. Environ. 146, 63–76.

Ryu J-H, Han H-J, Cho S, Park Y-J, Ahn Y-H, 2012. Overview of geostationary ocean color imager (GOCI) and GOCI data processing system (GDPS). Ocean Science Journal 47, 223–233.

Saimundsson P, 1986. Atmospheric refraction. Sky and Telescope 72, 70.

Salisbury J, Davis C, Erb A, Hu C, Gatebe C, Jordan C, Lee Z, Mannino A, Mouw C, Schaaf C, Schaeffer B, Tzortziou M, 2016. Coastal observations from a new vantage point. Eos 97.

Salisbury JE, Jonsson BF, Mannino A, Kim W, Goes JI, Choi JY, Concha JA, 2021. Assessing net growth of phytoplankton biomass on hourly to annual time scales using the Geostationary Ocean color instrument. Geophys. Res. Lett. 48.

Schaeffer BA, Myer MH, 2020. Resolvable estuaries for satellite derived water quality within the continental United States. Remote Sensing Letters 11, 535–544.

Schaeffer BA, Hagy JD, Conmy RN, Lehrter JC, Stumpf RP, 2012. An approach to developing numeric water quality criteria for coastal waters using the SeaWiFS satellite data record. Environ. Sci. Technol. 46, 916–922. [PubMed: 22192062]

Schaeffer BA, Whitman P, Conmy R, Salls W, Coffer M, Graybill D, Lebrasse MC, 2022. Potential for commercial PlanetScope satellites in oil response monitoring. Mar. Pollut. Bull. 183, 114077.

Seneviratne SI, Zhang X, Adnan M, Badi W, Dereczynski C, Luca AD, Ghosh S, Iskandar I, Kossin J, Lewis S, Otto F, Pinto I, Satoh M, Vicente-Serrano SM, Wehner M, Zhou B, 2021. Weather and Climate Extreme Events in a Changing Climate. In: Masson-Delmotte V, Zhai P, Pirani A, Connors SL, Péan C, Berger S, Caud N, Chen Y, Goldfarb L, Gomis MI, Huang M, Leitzell K, Lonnoy E, Matthews JBR, Maycock TK, Waterfield T, Yelekçi O, Yu R, Zhou B (Eds.), Climate Change 2021: The Physical Science Basis. Contribution of Working Group I to the Sixth Assessment Report of the Intergovernmental Panel on Climate Change, New York, NY, USA, pp. 1513–1766.

Seo S, Park YG, Kim K, 2020. Tracking flood debris using satellite-derived ocean color and particle-tracking modeling. Mar. Pollut. Bull. 161, 111828.

Seuront L, Lagadeuc Y, 1997. Characterisation of space-time variability in stratified and mixed coastal waters (Baie des Chaleurs, Québec, Canada):application of fractal theory. Mar. Ecol. Prog. Ser. 159, 81–95.

Shin J, Lee JS, Jang LH, Lim J, Khim BK, Jo YH, 2021. Sargassum detection using machine learning models: a case study with the first 6 months of GOCI-II imagery. Remote Sens. 13.

Soler T, Eisemann DW, 1994. Determination of look angles to geostationary communication satellites. J. Surv. Eng. 120, 115–127.

Stroming S, Robertson M, Mabee B, Kuwayama Y, Schaeffer B, 2020. Quantifying the human health benefits of using satellite information to detect cyanobacterial harmful algal blooms and manage recreational advisories in U.S. lakes. GeoHelath 4 (9), e2020GH000254.

Sun S, Hu C, 2016. Sun glint requirement for the remote detection of surface oil films. Geophys. Res. Lett. 43, 309–316.

Sun S, Hu C, Feng L, Swayze GA, Holmes J, Graettinger G, MacDonald I, Garcia O, Leifer I, 2016. Oil slick morphology derived from AVIRIS measurements of the Deepwater horizon oil spill: implications for spatial resolution requirements of remote sensors. Mar. Pollut. Bull. 103, 276–285. [PubMed: 26725867]

Sun S, Lu Y, Liu Y, Wang M, Hu C, 2018. Tracking an oil tanker collision and spilled oils in the East China Sea using multisensor day and night satellite imagery. Geophys. Res. Lett. 45, 3212–3220.

Svejkovsky J, Hess M, Muskat J, Nedwed TJ, McCall J, Garcia O, 2016. Characterization of surface oil thickness distribution patterns observed during the Deepwater horizon (MC-252) oil spill with aerial and satellite remote sensing. Mar. Pollut. Bull. 110, 162–176. [PubMed: 27389454]

Temitope Yekeen S, Balogun A-L, 2020. Advances in remote sensing technology, machine learning and deep learning for marine oil spill detection, prediction and vulnerability assessment. Remote Sens. 12.

Tzortziou M, Neale PJ, Megonigal JP, Pow CL, Butterworth M, 2011. Spatial gradients in dissolved carbon due to tidal marsh outwelling into a Chesapeake Bay estuary. Mar. Ecol. Prog. Ser. 426, 41–56.

Wang M, Bailey SW, 2001. Correction of sun glint contamination on the SeaWiFS ocean and atmosphere products. Appl. Opt. 40, 4790–4798. [PubMed: 18360519]

Wang S, Zhang X, Chen N, Wang W, 2022. Classifying diurnal changes of cyanobacterial blooms in Lake Taihu to identify hot patterns, seasons and hotspots based on hourly GOCI observations. J. Environ. Manag. 310, 114782.

Wang ZH, Bai Y, He XQ, Tao BY, Li T, Chen XY, Wang TY, Gong F, 2021. Estimating particulate organic carbon flux in a highly dynamic estuary using satellite data and numerical modeling. Remote Sens. Environ. 252.

Wheeler BW, White M, Stahl-Timmins W, Depledge MH, 2012. Does living by the coast improve health and wellbeing? Health Place 18, 1198–1201. [PubMed: 22796370]

Wittman AD, 1997. Astronomical refraction: formulas for all zenith distances. Astronomical Notes 318, 305–312.

Wu J, Goes JI, Gomes HDR, Lee Z, Noh JH, Wei J, Shang Z, Salisbury J, Mannino A, Kim W, Park YJ, Ondrusek M, Lance VP, Wang M, Frouin R, 2022. Estimates of diurnal and daily net primary productivity using the Geostationary Ocean color imager (GOCI) data. Remote Sens. Environ. 280, 113183.

Xing QW, Yu HM, Yu HQ, Wang H, Ito SI, Yuan CX, 2021. Evaluating the spring-neap tidal effects on chlorophyll-a variations based on the geostationary satellite. Front. Mar. Sci. 8.

Yang C-S, Bae S-S, Han H-J, Ahn Y-H, Ryu J-H, Han T-H, Yoo H-R, 2010. Introduction of acquisition system, processing system and distributing service for Geostationary Ocean Color Imager (GOCI) data. Korean Journal of Remote Sensing 26, 263–275.

Zhang J, Phaneuf DJ, Schaeffer BA, 2022. Property values and cyanobacterial algal blooms: evidence from satellite monitoring of Inland Lakes. Ecol. Econ. 199.

Zhang Y, Xu ZT, Yang YZ, Wang GF, Zhou W, Cao WX, Li Y, Zheng WD, Deng L, Zeng K, Zhang YX, 2021. Diurnal variation of the diffuse attenuation coefficient for downwelling irradiance at 490 nm in coastal East China Sea. Remote Sens. 13.

Zhao M, Bai Y, Li H, He XQ, Gong F, Li T, 2022. Fluorescence line height extraction algorithm for the Geostationary Ocean Color Imager. Remote Sens. 14, 2511.

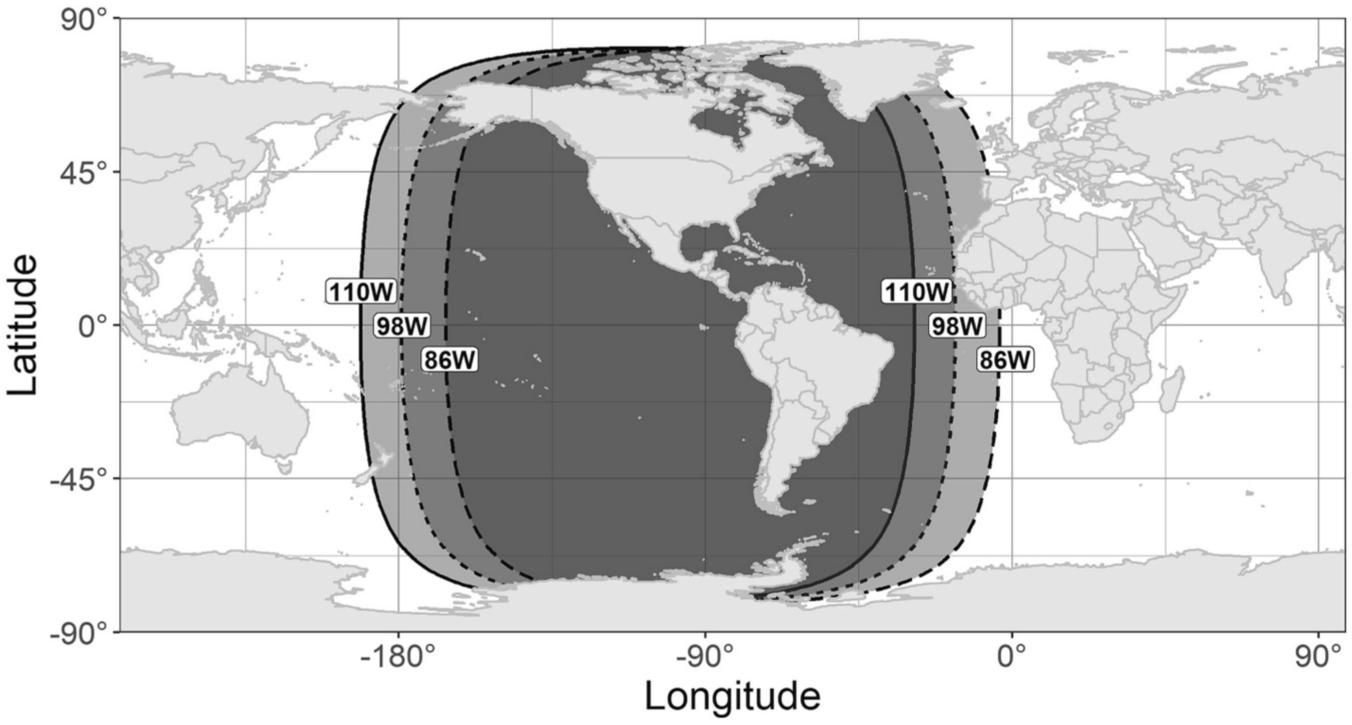

Fig. 1.

GLIMR field of regard centered at 110°, 98°, and 86° W longitude. Results throughout are based on a field of regard centered at 98°.

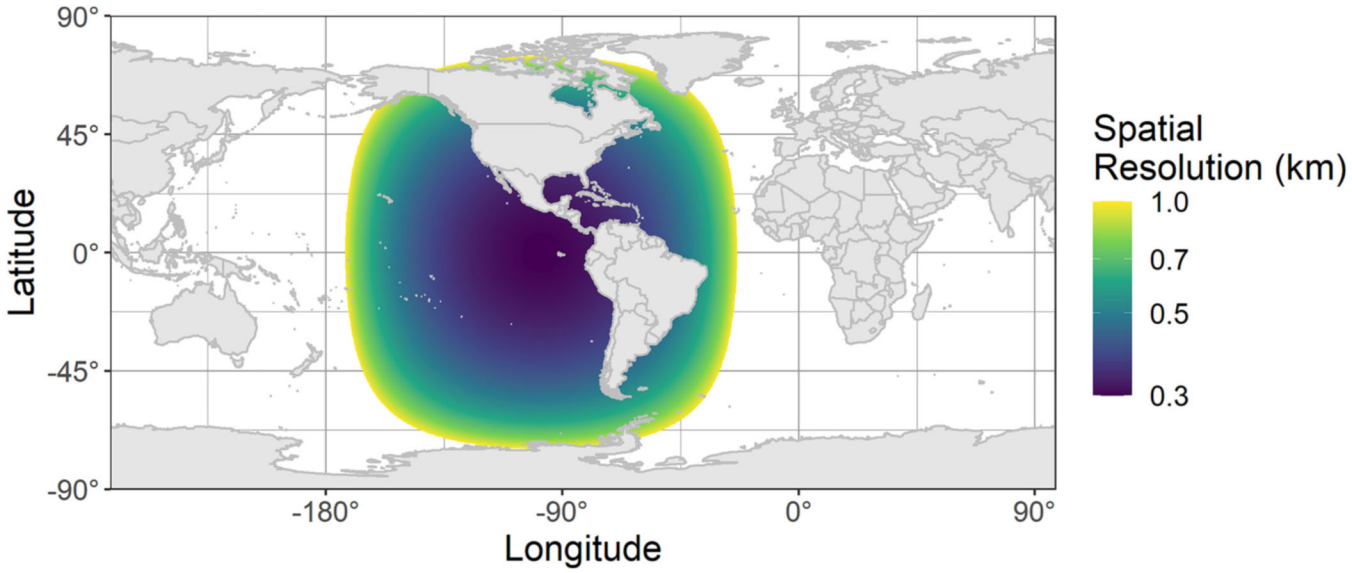

Fig. 2.

GLIMR spatial pixel resolution for 98° W longitude position where highest resolution was 300 m at nadir and increased above 1 km along the field of regard perimeter. GLIMR instantaneous field of view on detector is 300 m × 300 m with a 27-μm slit at 12.6 μrad in E to W direction. Overall spatial resolution performance is predicted to be 14.5 × 11.5 μrad.

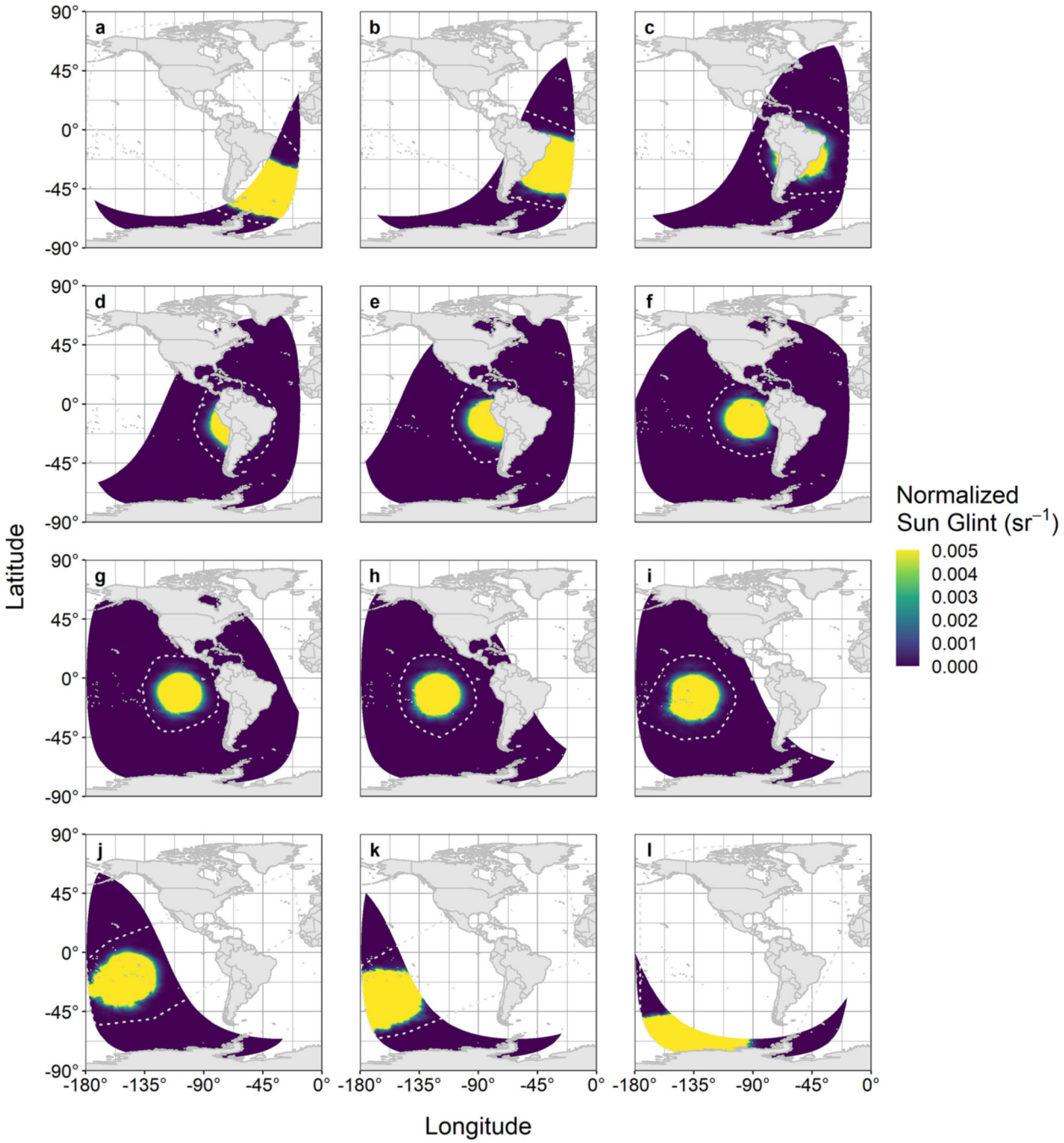

Fig. 3.

GLIMR December solstice sun glint with climatological winds. White dashed line represents glint threshold above 10^{-5} sr^{-1}, a threshold previously defined for oil spill film detection. The area in yellow represents where a high glint quality flag >0.005 sr^{-1} would mask observations of other water quality derived measures. Tiles (a) through (l) are 2-h increments of Coordinate Universal Time (UTC) starting with GLIMR sunrise at (a) 08:00 UTC through 24:00 UTC (i) and concludes before sunrise the next day at (l) 06:00 UTC.

(For interpretation of the references to color in this figure legend, the reader is referred to the web version of this article.)

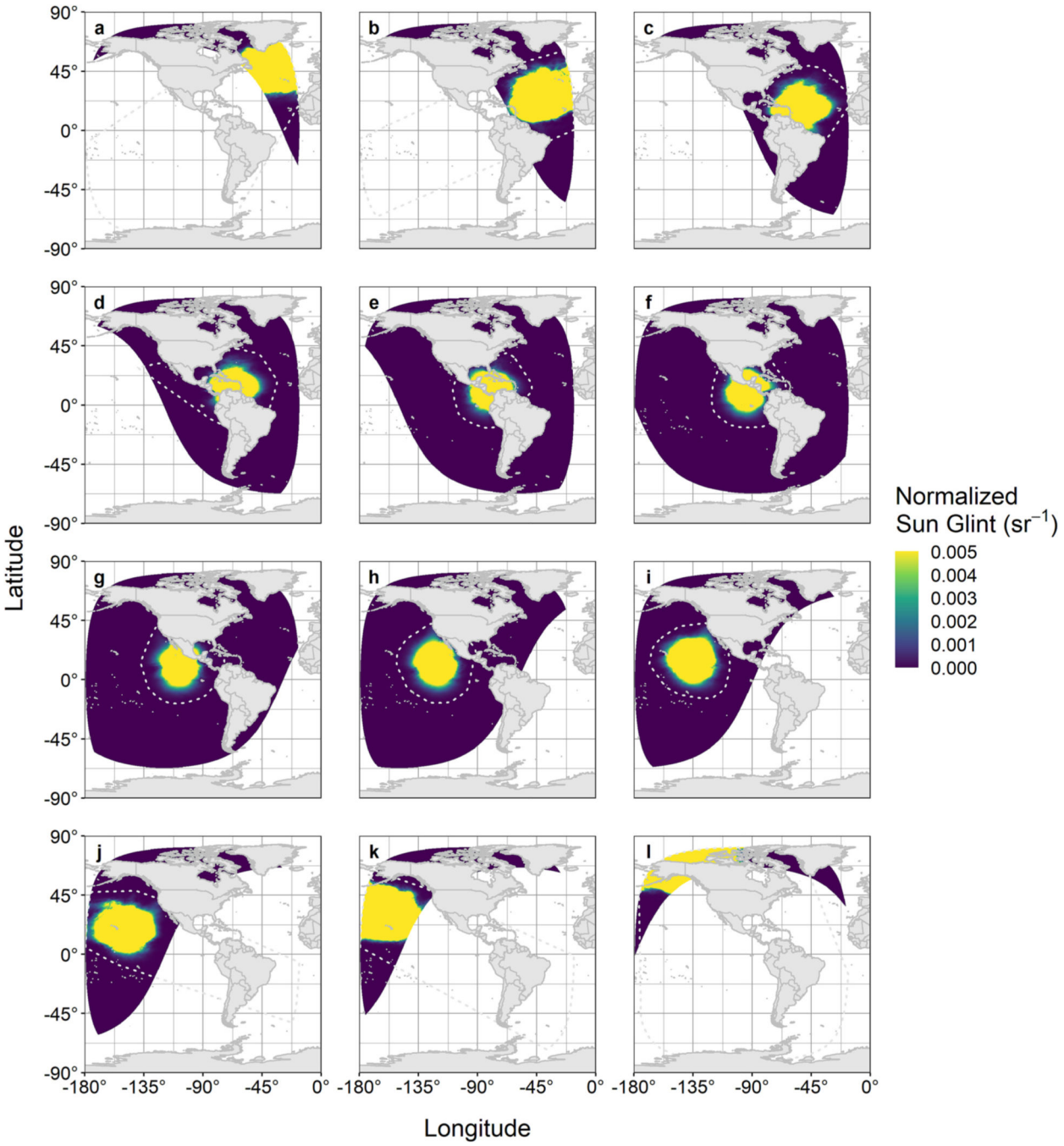

Fig. 4.

GLIMR June solstice sun glint with climatological winds. White dashed line represents glint threshold above 10^{-5} sr^{-1}, a threshold previously defined for oil spill film detection. The area in yellow represents where a high glint quality flag >0.005 sr^{-1} would mask observations of other water quality derived measures. Tiles (a) through (l) are 2-h increments of Coordinate Universal Time (UTC) starting with GLIMR sunrise at (a) 08:00 UTC through 24:00 UTC (i) and concludes before sunrise the next day at (l) 06:00 UTC. (For

interpretation of the references to color in this figure legend, the reader is referred to the web version of this article.)

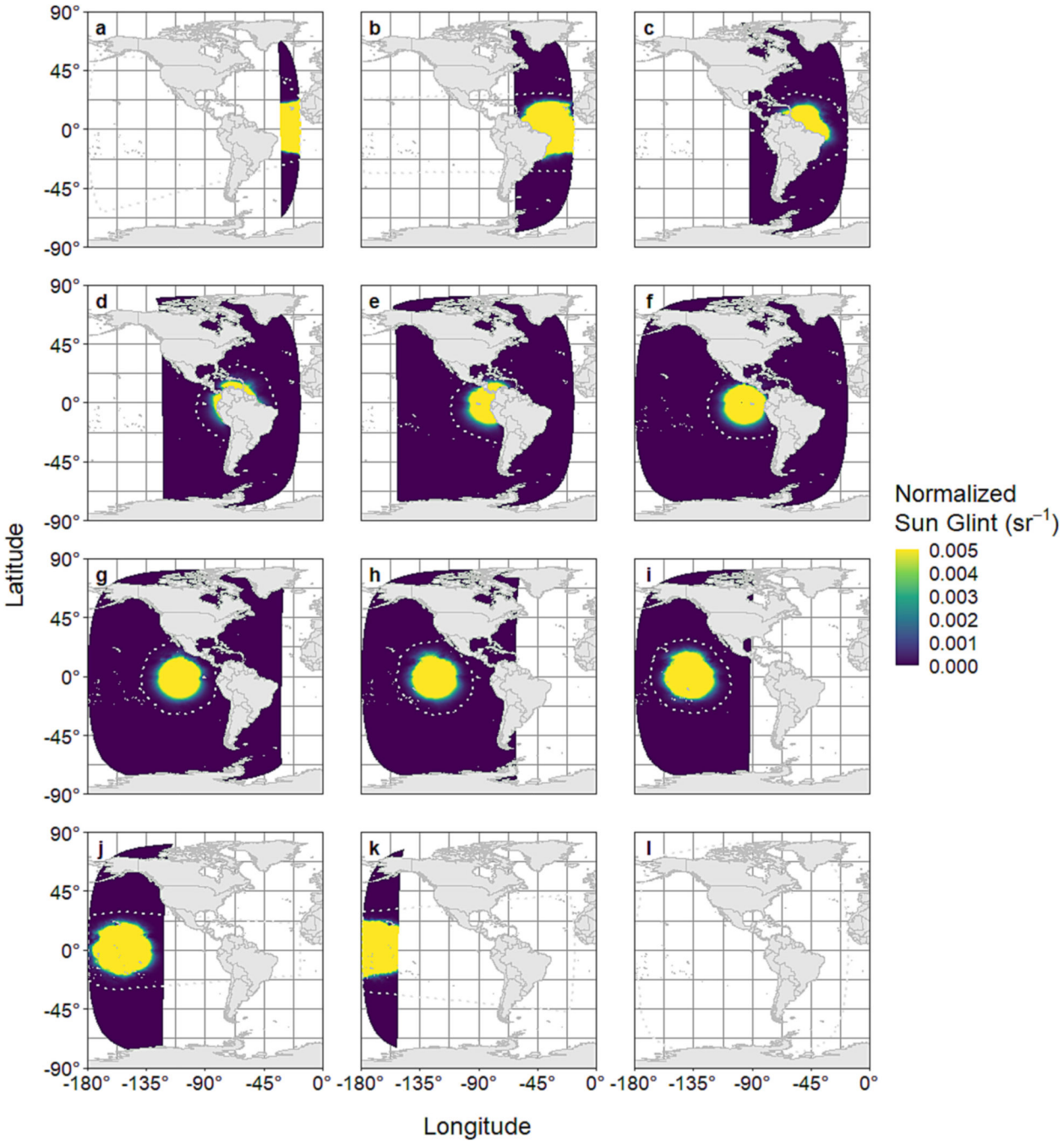

Fig. 5.

GLIMR March and September equinox sun glint with climatological winds. White dashed line represents glint threshold above 10^{-5} sr^{-1}, a threshold previously defined for oil spill film detection. The area in yellow represents where a high glint quality flag >0.005 sr^{-1} would mask observations of other water quality derived measures. Tiles (a) through (l) are 2-h increments of Coordinate Universal Time (UTC) starting at 00:00 UTC through 22:00 UTC. (For interpretation of the references to color in this figure legend, the reader is referred to the web version of this article.)

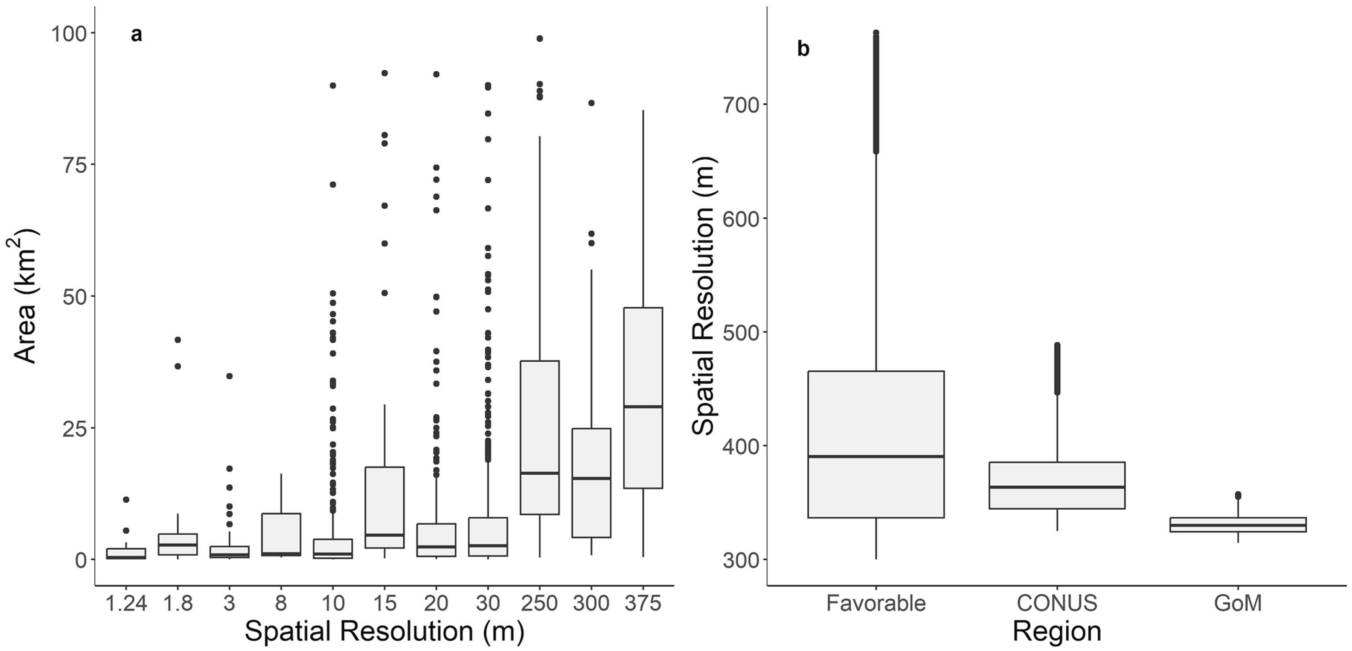

Fig. 6.

(a) Spatial resolution of optical satellites and reported oil spill areas from 1325 NOAA marine pollution surveillance reports between 2011 and 2021. Increase oiled area with coarser resolution satellites was due to the coverage area difference, where coarser resolution satellites covered larger areas than higher resolution satellites. (b) The spatial resolution for the favorable viewing area of 50° N to 50° S and 40° W to 155° W at the geostationary orbit of 98° W, CONUS, and Gulf of Mexico.

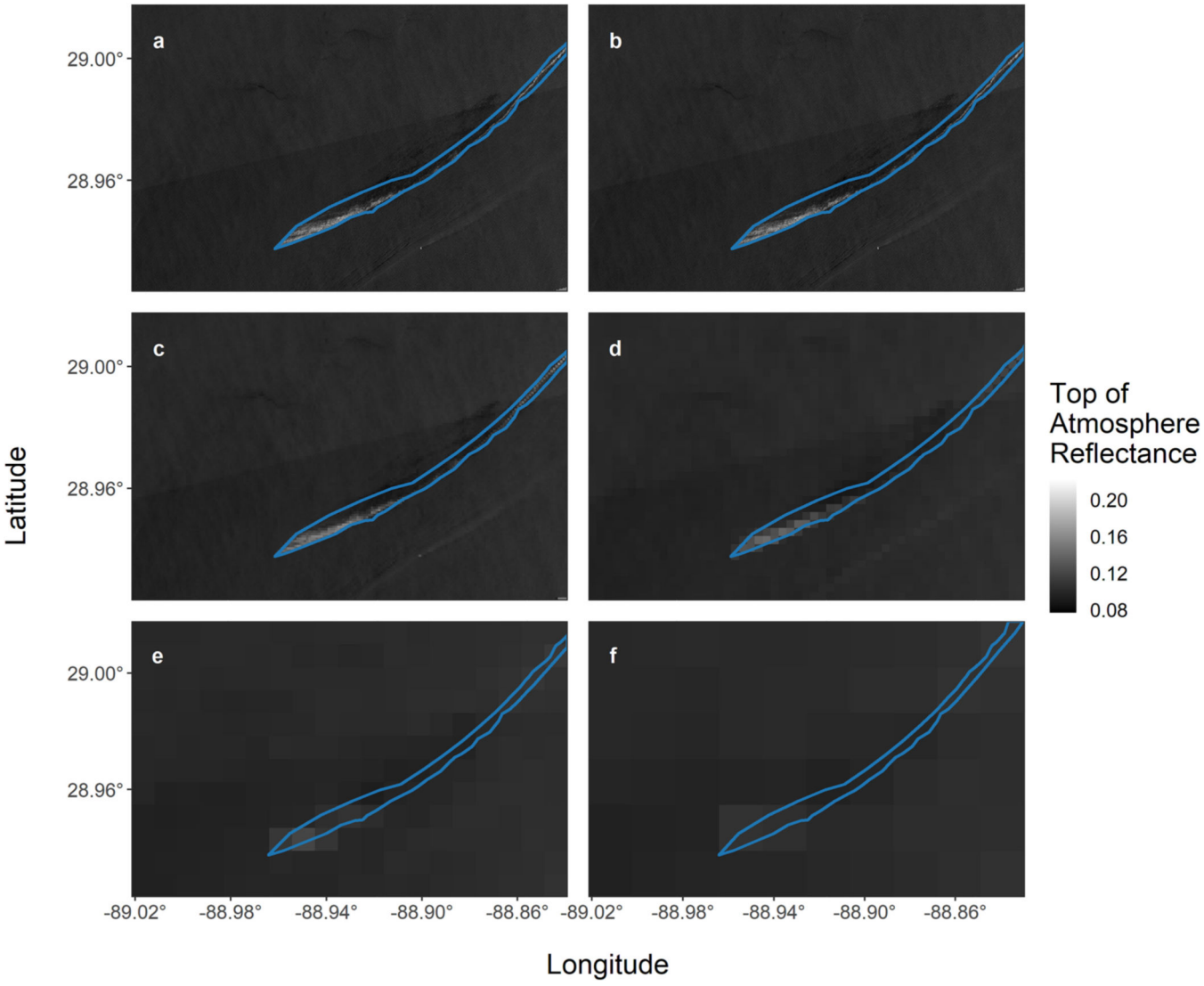

Fig. 7.

True color image (© Planet Labs Inc. 2019 all rights reserved) from PlanetScope at the Mississippi Canyon Block 20 Saratoga Platform (MC20) site near the Mississippi River Delta and 18 km off the coast of Louisiana, on August 6th, 2017. Decreasing spatial resolution was computed through resampling of a (a) 3.7 m PlanetScope image to (b) 4 m, (c) 40 m, (d) 400 m, (e) 800 m, and (f) 2000 m resolution at the MC20 site.

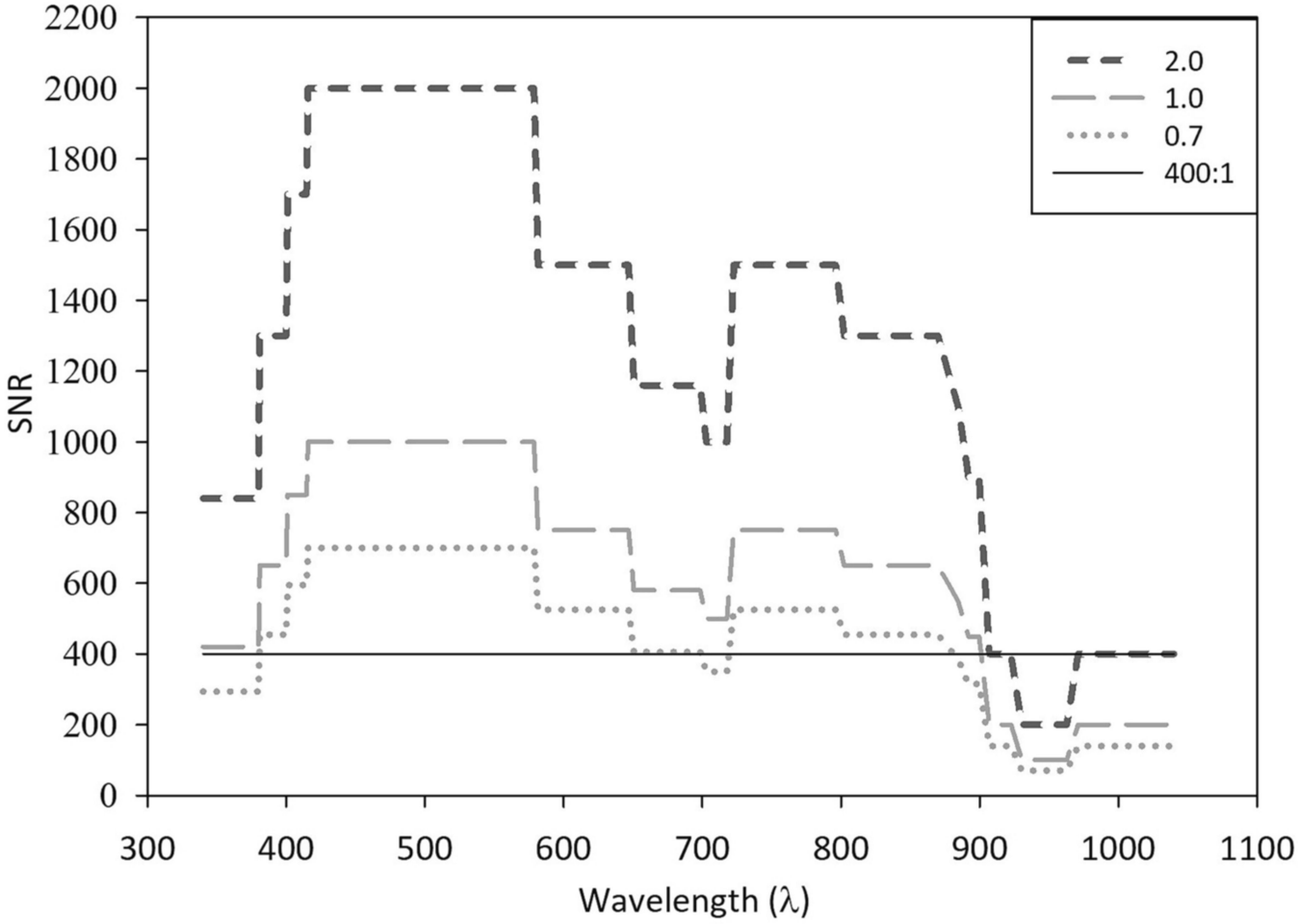

Fig. 8.

The current signal-to-noise ratio (SNR) as a function of wavelength given various SNR cases, where 1.0 is the default ocean color scan time requirement of 0.763 s. A factor of 0.7 would reduce the SNR to 400:1 from 650 to 700 nm, sufficient for the presence and absence detection of oil films and *Sargassum*. A doubling factor of the scan time increased SNR for low signal water quality events or to reduce observation uncertainty.

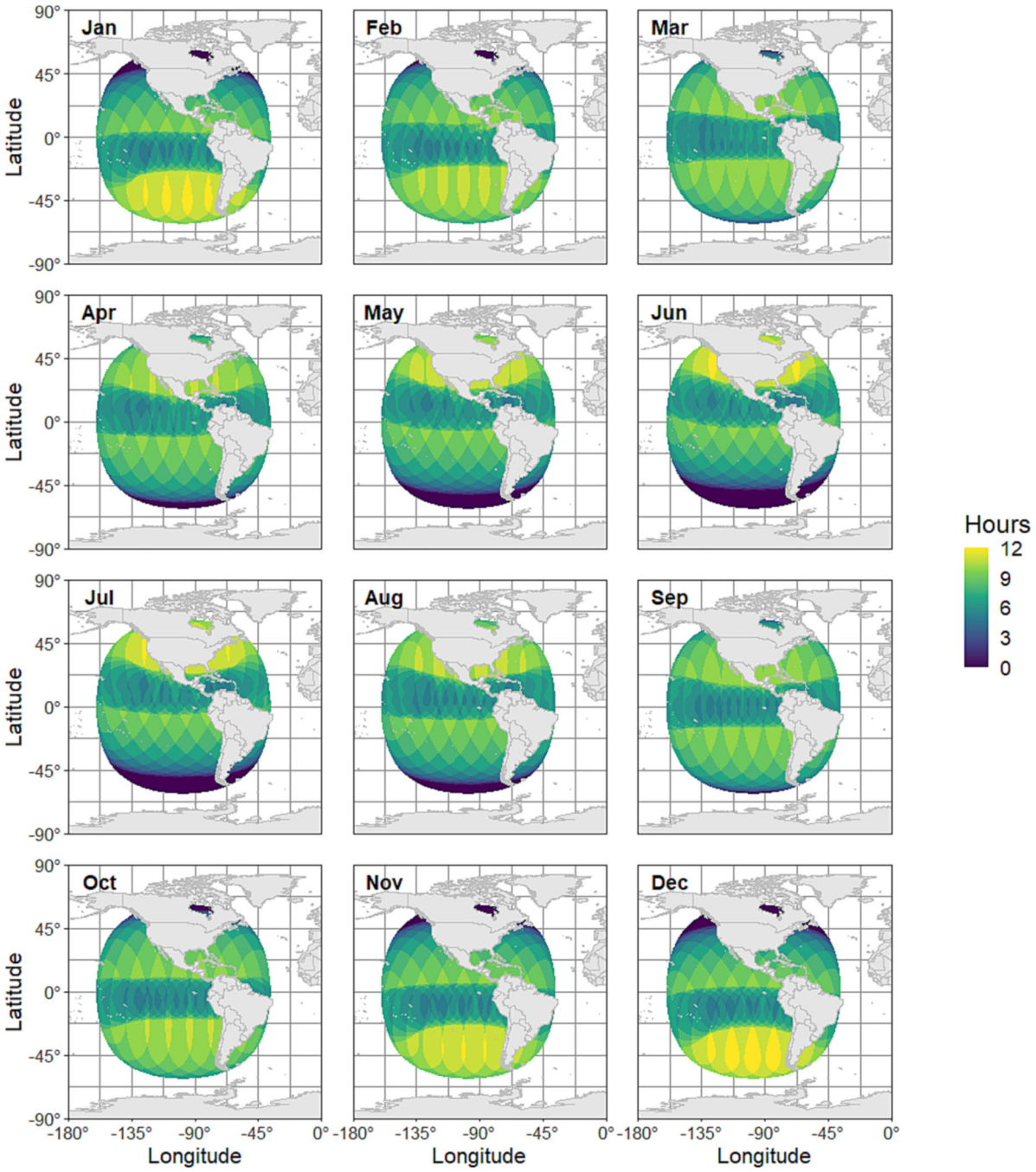

Fig. 9.

Average number of hours per day that a quality observation could theoretically be captured for ocean color water quality applications given climatological wind speed, sun glint, and an air mass fraction within 4.0 each month. Cloud interference was not considered in this analysis and has been previously reported by Feng et al. (2017), Mercury et al. (2012), and Schaeffer et al. (2022). Concentric pattern was a result of the 1-h model interval. Observation area was smaller than original field of regard because of 70° viewing angle cut off.

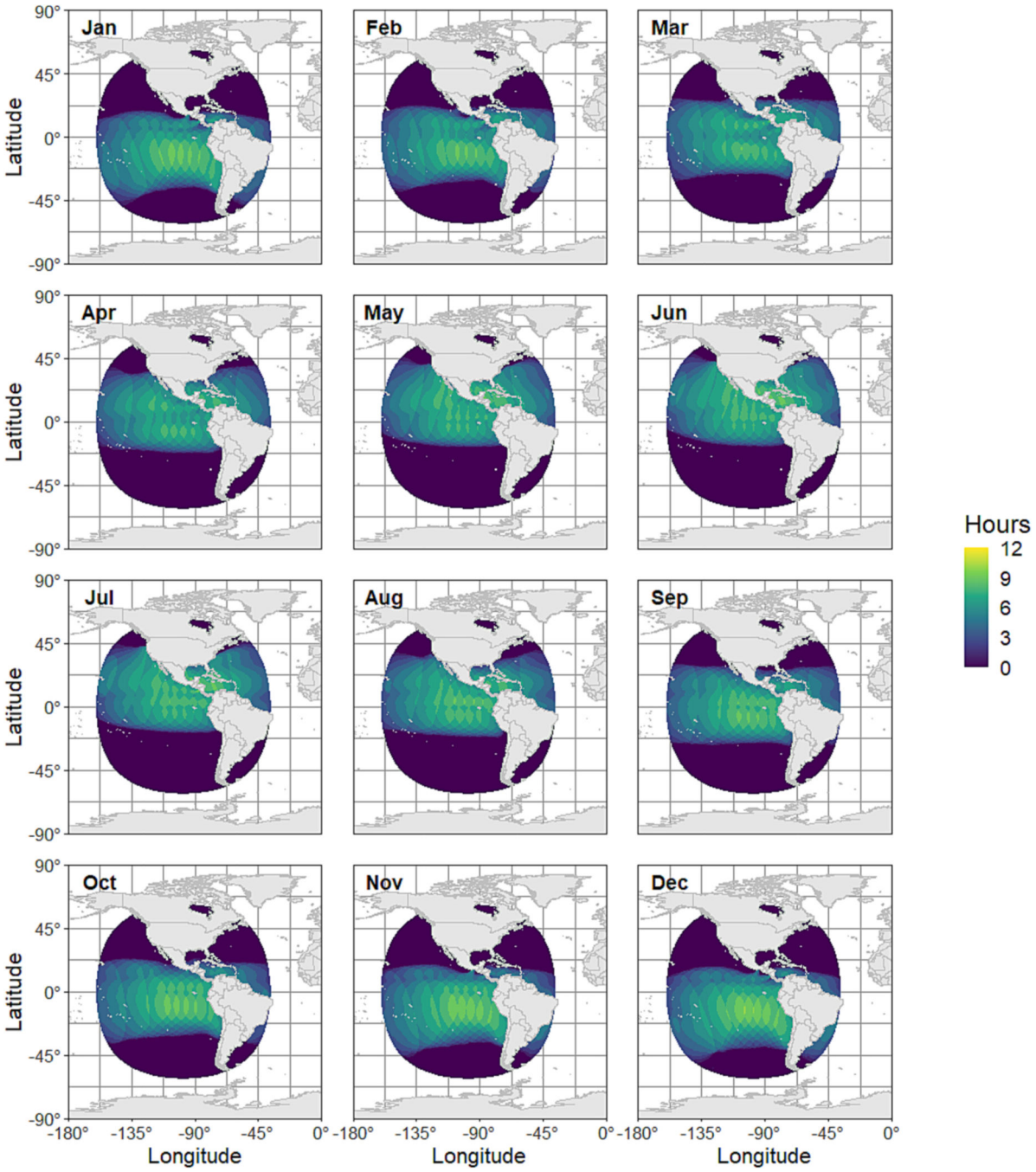

Fig. 10.

Average number of hours per day that a quality observation could theoretically be captured for oil film applications given climatological wind speed, sun glint, and an air mass fraction within 4.0 each month. Cloud interference was not considered in this analysis and has been previously reported by Feng et al. (2017), Mercury et al. (2012), and Schaeffer et al. (2022). Concentric pattern was a result of the 1-h model interval. Observation area was smaller than original field of regard because of 70° viewing angle cut off.

Table 1

Summary of symbols and definitions in calculating normalized sun glint for GLIMR.

Symbol	Units	Name	Definition
L_{GN}	sr^{-1}	Normalized sun glint	Sun glint radiance received by a sensor regardless of incident solar radiance.
p		Slope probability density function	A function of the viewing geometry and sea surface roughness variance that contribute to sun glint.
θ	Degrees	Sensor zenith angle	Angle of the satellite relative to a vertical line above the observation point.
$\rho(\omega)$	Unitless	Fresnel reflection coefficient	Fixed coefficient describing the interaction between unpolarized light and the water surface.
β	Degrees	Surface tilt	The angle of reflection on a facet on the sea surface with a particular orientation that reflects sunlight to the satellite
σ^2	Unitless	Sea surface roughness variance	sensor relative to a horizontal plane. Measure of waves at the sea surface.
θ_0	Degrees	Solar zenith angle	Angle of the sun relative to a vertical line above the observation point.
ϕ	Degrees	Azimuth angle	Angle between the sensor and the sun
W	$m\ s^{-1}$	Wind speed	relative to the observation point. The horizontal speed of air moving in any direction at an altitude of 10 m
μ	$m\ s^{-1}$	Eastward wind	above the Earth. The horizontal speed of air moving towards the east at an altitude of 10 m
υ	$m\ s^{-1}$	Northward wind	above the Earth. The horizontal speed of air moving towards the north at an altitude of 10 m above the Earth.

Table 2

GLIMR scan time based on a swath width for existing and future polar orbiting platforms. The larger the swath width, the longer it would take GLIMR to rescan the equivalent area. The region of interest location impacts GLIMR's scan time, where the further from GLIMR's nadir point, the shorter the scan time.

Mission	Sub-satellite point	Latitude			Longitude		
	0°N, −98°W	±20°	±40°	±60°	±20°	±40°	±60°
VIIRS (3000 km)	125.07	123.49	119.14	112.83	123.80	105.22	70.53
PACE (2663 km)	111.36	109.96	106.15	100.65	109.64	91.69	60.02
Sentinel-3 (1270 km)	53.60	52.94	51.13	48.67	50.98	39.74	23.28
Sentinel-2 (290 km)	12.27	12.12	11.71	11.18	11.25	8.33	4.44
Landsat (185 km)	7.85	7.74	7.49	7.13	7.15	5.26	2.77
Planetscope (24 km)	1.03	1.00	0.98	0.93	0.93	0.67	0.36
Legion (9 km)	0.39	0.39	0.37	0.37	0.36	0.25	0.14